



Opal-based terahertz optical elements fabricated by self-assembly of porous SiO₂ nanoparticles

V. E. ULITKO,^{1,6} G. M. KATYBA,^{1,2,3} V. A. ZHELNOV,^{2,3} I. M. SHMYTKO,¹ G. A. EMELCHENKO,¹ I. E. SPECTOR,² V. M. MASALOV,¹ V. N. KURLOV,^{1,3,4} K. I. ZAYTSEV,^{2,3,4,7}  AND M. SKOROBOGATIY^{5,8} 

¹*Institute of Solid State Physics of the Russian Academy of Sciences, Russia*

²*Prokhorov General Physics Institute of the Russian Academy of Sciences, Russia*

³*Bauman Moscow State Technical University, Russia*

⁴*Institute for Regenerative Medicine, Sechenov First Moscow State Medical University (Sechenov University), Russia*

⁵*Department of Engineering Physics, Polytechnique Montreal, Canada*

⁶*ulitko.vl@gmail.com*

⁷*kirzay@gmail.com*

⁸*maksim.skorobogatiy@polymtl.ca*

Abstract: In this paper, we study artificial opals as a promising material platform for terahertz (THz) optics. Materials were synthesized using self-assembly of porous SiO₂ nanoparticles and annealing at different temperatures to further tune their optical properties. Two distinct approaches for the fabrication of bulk THz optics from these novel materials were considered. First, THz cylindrical lenses of identical geometry but different refractive indices and focal lengths were produced using standard mechanical processing of opals, in order to highlight their compatibility with conventional technologies of bulk optics fabrication. Second, a THz axicone was made via direct sedimentation of aqueous colloidal suspension of SiO₂ nanoparticles in the mold of geometry inverse to that of a desired optical shape, followed by annealing and polishing. The second approach has an advantage of being considerably less labor intensive, while capable of obtaining optical elements of complex geometries. Thus fabricated bulk THz optical elements were studied experimentally using continuous-wave THz imaging, and the results were compared with 2D and 3D numerical predictions based on the finite-difference time-domain and finite-element frequency-domain methods. Our findings highlight technological robustness of the developed THz optical material platform and, thus, open the door for creating a variety of bulk THz optical elements of complex shapes and widely-tunable optical performance.

© 2021 Optical Society of America under the terms of the [OSA Open Access Publishing Agreement](#)

1. Introduction

Today, terahertz (THz) spectroscopy and imaging [1] constitute important tools for applications in astrophysics [2,3], biomedicine [4,5], condensed matter physics [6,7], chemical and pharmaceutical industries [8], materials science and non-destructive testing [9], security [10], and food science [11]. Despite a rapid progress, THz science and technology remain a fairly new branch of optics that can still profit from advanced optoelectronic components, optical systems and materials [12–14]. Therefore, development of novel THz optical materials and related fabrication and processing techniques remains an active research field [15–17].

Among the available THz optical materials, polymers are probably the most abundant [18]. Polymer-based bulk and fiber THz optics profit from the well-developed techniques, such as polymer drawing, compression molding, and 3D printing [19–28]. Another group of common

THz optical materials is formed by various crystalline media [29]. However, mechanical processing of such materials is challenging due to their hardness, high melting point, and (in some cases) anisotropy of physical properties; therefore, a variety of processing techniques have been developed to mold them into complex shapes. Among the crystalline materials, sapphire (α -Al₂O₃) is particularly suitable for fabrication of the THz waveguide and fiber optics thanks to its compatibility with the edge-defined film-fed growth technique [30–32]. Such a technique enables fabrication of sapphire shaped crystals with pre-determined complex cross-sections from the Al₂O₃-melt without the need for mechanical processing [33]. The versatility of this technique was recently demonstrated when fabricating flexible sub-millimeter-diameter step-index sapphire fibers [34,35], sapphire optical fiber bundles [36], hard photonic crystal and antiresonant sapphire waveguides [37–39].

Another promising material platform for THz applications comprises various nano- and micro-porous materials and composites [40–44], thanks to their low-to-moderate THz-wave absorption, as well as wide-range tunability of their optical properties by varying the material porosity and composition. For example, in Ref. [27], lens for THz-beam focusing and phase plate for generation of angular momentum beams were fabricated by laser cutting of polymethylpentene (TPX) flats with gradient radial and angular distribution of pores over their optical aperture. In Ref. [23], additive manufacturing was used to print a gradient-refractive-index THz lens. While these computer-assisted manufacturing approaches can yield a variety of complex THz optical elements, they are limited to use of suboptimal (for THz optics) materials, that are compatible with such manufacturing techniques, they require expensive infrastructure, and lack in resolution

Recently [17,45,46], nanoporous SiO₂ based on artificial opals annealed at different temperatures was studied as a prospective material platform for THz optics. A combination of THz pulsed spectroscopy, X-ray diffractometry, scanning electron microscopy and porosity measurements (using a hydrostatic weighting technique) revealed that optical properties of such materials can be tuned in a wide range by annealing. Namely, the refractive index changes from 1.6 to 1.95, while the amplitude absorption coefficient decreases from 7 to 1 cm⁻¹ at 1.0 THz with increasing annealing temperature. Such a wide tunability of optical properties, low-to-moderate THz-wave absorption and mechanical robustness of such materials make them attractive for fabrication of various THz optical elements. Generally, in order to achieve a particular THz refractive index of the nanoporous SiO₂-based optical element, one should simply use an appropriate annealing temperature (tabulated in a calibration measurement) during manufacturing. Otherwise, when the THz refractive index of the optical material is not of prime importance, one can resort to higher annealing temperatures to minimize the THz-wave absorption losses.

In this paper, we report design, fabrication, and characterization of THz optical elements based on nanoporous SiO₂. Two experimental techniques were developed for manufacturing bulk THz optical elements from the considered material platform. Firstly, two cylindrical THz lenses with identical geometry were fabricated, using standard mechanical processing, from distinct pieces of opal-based nanoporous SiO₂, that were annealed at the temperatures of 900 and 1200°C, respectively. The two lenses feature different refractive indices and focal lengths. Secondly, a THz axicone was produced via direct sedimentation of aqueous colloidal suspension of the porous SiO₂ nanoparticles onto a substrate, the geometry of which is inverse to that of a desired optical surface, followed by annealing and mechanical finishing. Optical properties of thus fabricated THz lenses and axicone were then characterized experimentally, using continuous-wave THz imaging, and numerically, using the 2D Finite-Difference Time-Domain (2D FDTD) and 3D Finite-Element Frequency-Domain (3D FEFD) methods of solving the Maxwell's equations. The observed experimental data agree well with the theoretical predictions. Our results highlight technological robustness of the considered THz optical material platform, paving the way for its use in fabrication of bulk THz optical elements having complex shapes and optical performance that is tunable over a wide parametric range.

2. Fabrication of the nanoporous SiO₂ optical elements

First, two types of monodispersed spherical porous SiO₂ nanoparticles of sized 300 and 600 nm were grown using the modified Stober-Fink-Bohn method [47,48]. Then, two distinct strategies were developed:

- For the fabrication of cylindrical lenses, we used bulk samples of artificial opals obtained by sedimentation of colloidal suspension of monodispersed spherical SiO₂ particles with the diameter of 300 nm. The opal samples were dried and annealed at the temperatures of 900 and 1200°C for 24 hours in order to achieve distinct THz refractive indexes of the annealed opals, as discussed in Ref. [17].
- For the fabrication of a THz axicon, 600-nm-diameter SiO₂ nanoparticles were used. In principle, within this methodology one can also use larger diameter nanoparticles of ~ 1 μm-diameter, which are still negligibly small at the THz-wavelength scale and, thus, not causing any sizeable increase in the material scattering losses in the THz range. At the same time, somewhat larger diameter nanoparticles allow considerable enhancement of the sedimentation rates in a mold [49], thus, speeding-up the fabrication of optical elements. Particularly, sedimentation rates for the 300-nm and 600-nm particles were estimated to be ~ 0.05 and ~ 0.167 mm/hour respectively, which constitutes an enhancement factor of 3 (for sedimentation rate) when increasing particle size.

Typical dimension of interglobular pores of opal matrix are ≈ 10 – 20 times smaller than the diameter of globules. As the dimensions of both types of nanoparticles (along with the dimensions of pores between them) are smaller than the THz wavelengths by several orders of magnitude, Mie scattering and, thus, related scattering losses of THz waves propagating through the resultant optical materials are greatly suppressed [17].

2.1. Fabrication of cylindrical lenses by mechanical processing

Bulk opal samples made of 300-nm-diameter nanoparticles and annealed at different temperatures were mechanically shaped into parallelograms for the following insertion into a grinding holder; see Fig. 1(a). The samples were rigidly fixed in the holder using acetone-soluble glue. The holder was then rotated and moved slowly toward the grinder stone in order to form cylindrical surface of the lenses in a multi-run regime. After shaping, lenses were removed from the holder using acetone and, then, cleaned in the ultrasound bath filled with acetone. In Fig. 1(b), we show 3D schematic of thus fabricated cylindrical lenses having the height of 10 mm, the width of 18 mm, and the curvature radius of 30 mm, which is defined during grinding by the cylindrical surface of the holder. A photo of the two fabricated lenses is shown in Fig. 1(c). While having identical geometries, the two lenses possess distinct refractive indices and, thus, focal lengths. From Fig. 1(c), we also notice that nanoporous SiO₂ materials annealed at distinct temperatures show different optical properties in the visible range. Namely, the 900°C-sample is optically opaque, while the 1200°C-one appears to be optically translucent. Despite the fact that both samples are in the same phase amorphous state [17], the one annealed at 1200°C has a porosity $\approx 0\%$ (by volume), as compared to a 900°C sample with the porosity of $\approx 30\%$, which results in a much reduced visible light scattering. A considerable different in porosity of the studied materials is evident from Fig. 1(d), where their Scanning-Electron Microscopy (SEM) images are presented; the latter were obtained using Zeiss Supra 50 VP SEM system. Both samples are mechanically robust, thus, allowing to produce bulk optical elements using conventional mechanical processing.

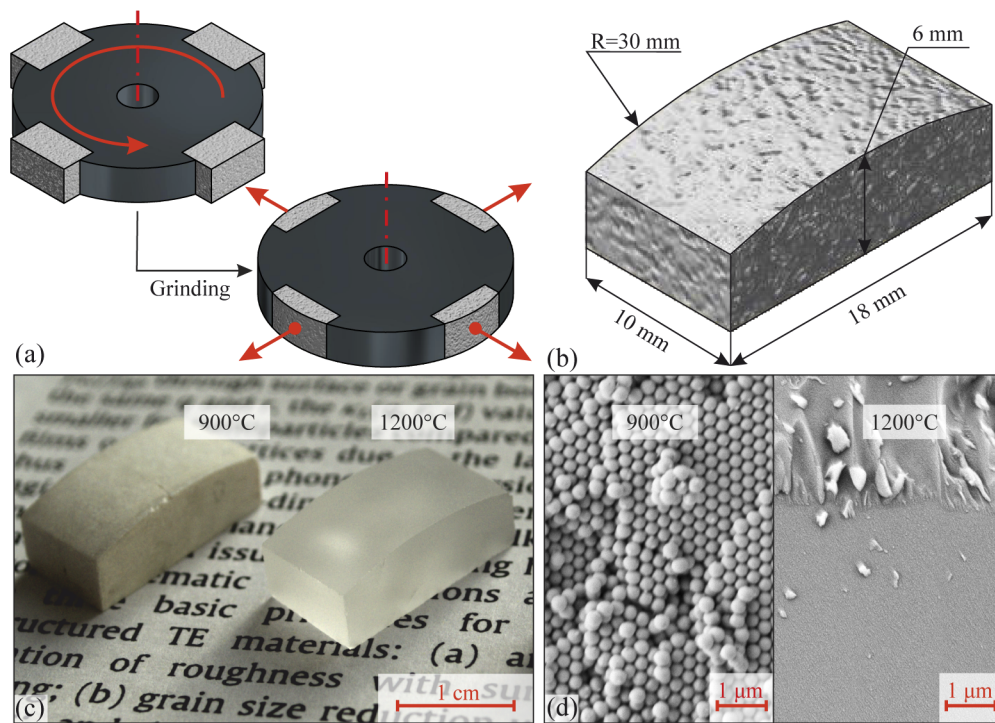


Fig. 1. Fabrication of the cylindrical convex-plane lenses by mechanical processing of bulk pieces of nanoporous SiO_2 . (a) Multirun grinding of the lenses using rotational holder, and Removal of lenses from the holder after grinding. (b) 3D schematic of a cylindrical lens. (c) Photo of the fabricated lenses made of two nanoporous SiO_2 materials, annealed at the temperatures of 900 and 1200°C and, thus, featuring different refractive indices and focal distances. (d) SEM images of the two nanoporous SiO_2 pieces made of 300-nm-diameter nanoparticles and annealed at the temperatures of 900 and 1200°C, respectively.

2.2. Fabrication of an axicon by direct sedimentation of colloidal suspension in a mold

As an alternative approach for the fabrication of THz optical components, we considered direct sedimentation of aqueous colloidal suspension into a mold with the geometry inverse to the desired shape of an optical element. To demonstrate the versatility of this method, we fabricated an axicon for generation of Bessel beams [50], that features a conical optical surface formed without resorting to mechanical processing.

Particularly, sedimentation of the 600-nm-diameter nanoparticles into a hollowed conical mold was used. The mold was machined from a bulk piece of PolyMethyl MethAcrylate (PMMA) using a turning lathe, and it features the internal diameter of 30 mm, the axial depth of 10 mm, and the apex angle of 160°. The apex of the mold and, thus, of the axicon optical surface is slightly rounded, but is not expected to impact considerably the optical element performance [51]. During the sedimentation process, the mold was mounted inside a 7.5-cm-tall tube filled with aqueous suspension of SiO_2 nanoparticles; see Fig. 2(a). The suspension concentration was $\approx 10\%$ (by volume), which resulted in the axicon thickness of ≈ 7.5 mm. After the sedimentation, the axicon was removed from the mold, dried and, then, annealed at the temperature of 950°C for 24 hours. During drying the sediment insignificantly shrinks; while during annealing the shrinkage was as much as $\approx 14\%$ (linear measure). It is worth noting that no cracking or other mechanical damage to the optical element was observed at these fabrication stages. Finally, after

drying and annealing, a small meniscus was removed from the top flat surface of the axicon using light polishing; see Fig. 2(b).

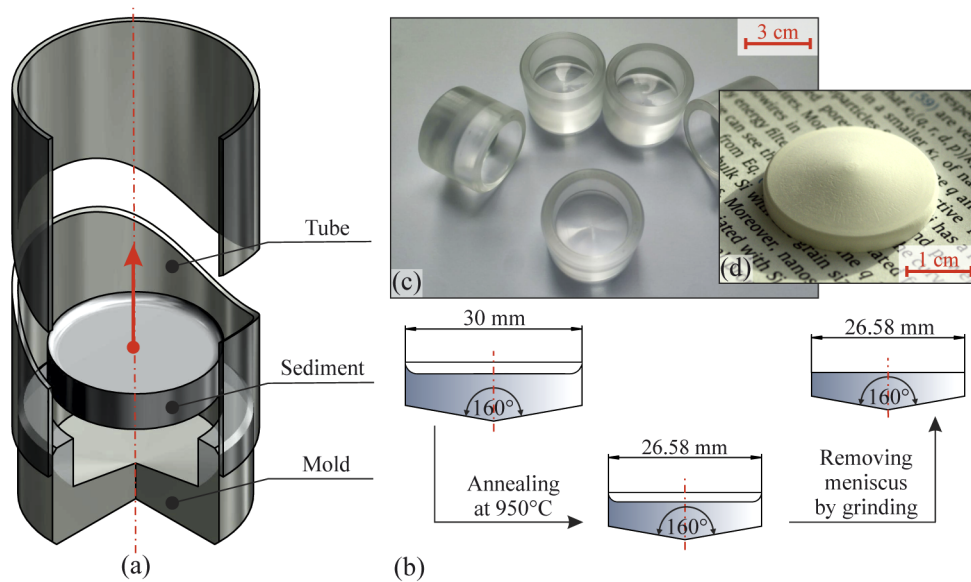


Fig. 2. Axicon fabrication via direct sedimentation of colloidal suspension of SiO₂ nanoparticles into a mold. (a) Schematic of the sedimentation setup comprising a mold and a tube filled with the $\approx 10\%$ aqueous suspension of nanoparticles. Red arrow shows the direction of the axicone removal after the sedimentation process. (b) Schematic of the axicone post-processing, including annealing at 950°C, that leads to the linear shrinkage of $\approx 14\%$, and light mechanical polishing, aimed at the removal of a meniscus. (c),(d) Photos of the PMMA molds and the final axicone.

In this way, a THz axicon with the resultant diameter of 26.58 mm and the apex angle of 160° was fabricated, as shown in Fig. 2(d).

3. Terahertz pulsed spectroscopy of the nanoporous SiO₂ flats

Before characterizing THz lenses and axicon, THz optical properties of bulk materials used in their fabrication were studied with the help of THz pulsed spectroscopy. To this aim, planar samples (flats) of thickness ~ 1 mm and surface area ~ 1 cm² were fabricated by grinding nanoporous SiO₂ pieces, which were synthesized using the same protocols as those used in the fabrication of THz optical elements.

A home-made THz pulsed spectrometer with a vacuum sample chamber (detailed in Refs. [52–54]) was used in our measurements, which were carried out in the transmission mode using focused THz beam; see Fig. 3(a). The measurements were performed with a sample placed atop of the metal diaphragm with the diameter somewhat larger than the THz beam spot, while the reference waveform was acquired with the empty diaphragm [17]. The sample optical properties were reconstructed in the frequency range of 0.2–2.5 THz using the well-known approach from Refs. [55,56], while the spectral resolution was ~ 0.03 THz.

Frequency-dependent refractive index n and absorption coefficient α (by field) of the three nanoporous SiO₂ flats are shown in Figs. 3(b) and (c). As clear from Fig. 3, refractive index of the considered materials increases with increasing annealing temperature due to reduced material porosity. The observed results agree with Ref. [17] and highlight wide-range optical tunability of nanoporous SiO₂ by annealing.

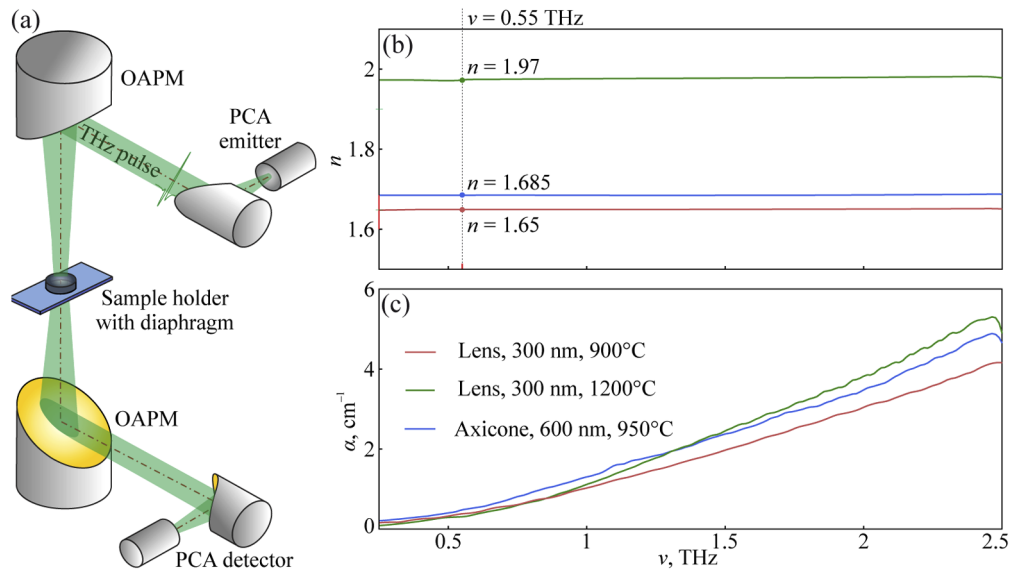


Fig. 3. THz pulsed spectroscopy of nanoporous SiO₂ flats fabricated using the same protocols as the corresponding THz optical elements. (a) Schematic of the THz pulsed spectrometer, where OAPM stands for an off-axis parabolic mirror, while PCA is a photoconductive antenna. (b),(c) Measured refractive indices n and absorption coefficients α (by field) of the flats. In (b), by vertical dashed line, we marked the frequency of 0.55 THz, at which the developed THz lenses and axicone are further studied numerically and experimentally in the continuous-wave regime.

4. Numerical modeling of the nanoporous SiO₂ optical elements

Two distinct methods of computational electrodynamics were used to model THz-wave propagation through optical elements at the frequency of $\nu \approx 0.55$ THz, or the free-space wavelengths of $\lambda = 545 \mu\text{m}$. This particular wavelength was selected to match that of the THz emitter used in the experimental studies.

First, infinitely long cylindrical lenses were studied using an in-house 2D FDTD method [57]. A classic Yee's approach was used for the spatial- and time-domain discretization of the simulated volume [58], with the spatial step of $\Delta_r = \lambda/100$ and the time-domain step satisfying the Courant-Friedrichs-Lewy condition $\Delta_t \leq \Delta_r/(c_0\sqrt{3})$ [57]; here, $c_0 = 3 \times 10^8$ m/s is the speed of light in free space. The Total-Field / Scattered-Field (TFSF) method was used to introduce a plane wave into the simulated volume [59]; while the 2nd-order Mur's absorption boundaries allowed for preventing unphysical back-scattering of waves from the edges of the simulated volume [57]. A plane electromagnetic wave irradiated a cylindrical lens from its convex side. Both Transverse Magnetic (TM), with the electric field vector \mathbf{E} perpendicular to the simulation plane, and Transverse Electric (TE), with \mathbf{E} in the simulation plane, polarization response [57] was studied, and essentially polarization-independent system performance was found. Here, only the TM polarized scattered field is considered without the loss of generality. Results of 2D simulations were then compared with 3D formulations.

For modeling of the Bessel beam formation behind the axicone, a quasi-3D FEFD method [60] within the COMSOL Multiphysics Software was applied profiting from the axial symmetry of this optical element. A quasi-3D FEFD method models optical systems with a rotational symmetry with respect to the set optical axis (OZ in our case), and is carried out using an optical system 2D cross-section in cylindrical coordinates (\mathbf{r}, z) ; where \mathbf{r} is a radius vector perpendicular

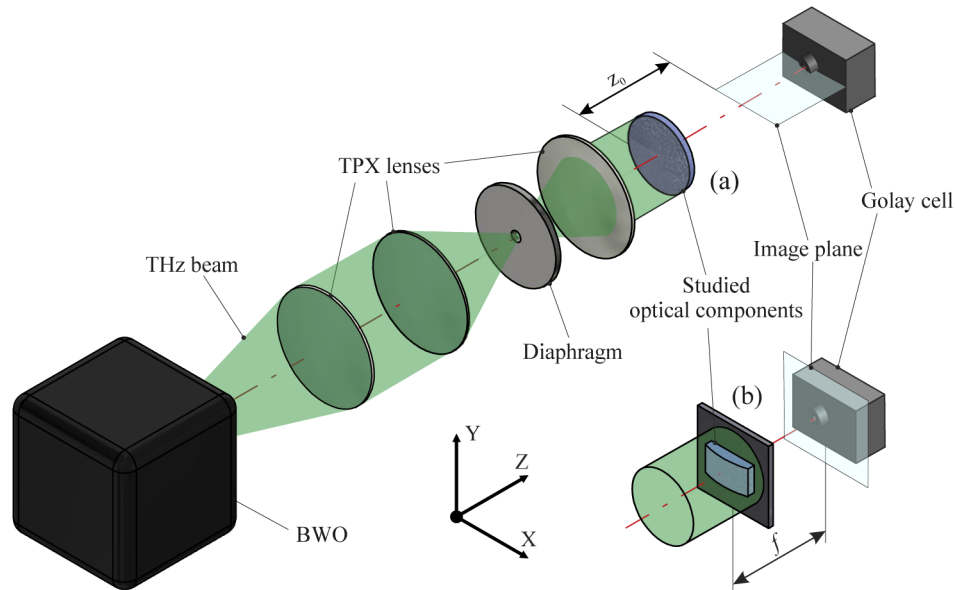


Fig. 4. Schematic of the continuous-wave THz imaging setup that is used for characterization of (a) an axicon and (b) cylindrical lenses made of nanoporous SiO_2 . In both (a) and (b), a linearly-polarized plane electromagnetic wave radiates an optical element from its convex side, while spatial distribution of the scattered THz field intensity $I(\mathbf{r})$ is measured at its shadow side.

to OZ axis. Cylindrical Perfectly-Matched-Layers (PML) were applied as absorbing boundaries at the simulation volume borders to prevent unphysical back-scattering into the simulation volume [57]. Within a quazi-3D analysis, an ideal electromagnetic plane wave of circular polarization and angular momentum $|m| = 1$ is introduced into simulation volume using the TFSF approach [59]. To model focal spot shape due to scattering of a linearly-polarized plane wave (used in the experiment), we first performed two simulations using circularly-polarized plane waves of angular momenta $m = 1$ and $m = -1$. We then coherently added thus obtained solution fields to get a solution corresponding to a linearly polarized plane wave excitation field. Furthermore, a 2D FEFD beam envelope method was used to compare properties of finite-length cylindrical lenses with those of infinite cylindrical lenses as predicted by 2D FDTD.

Both in the 2D-FDTD and 3D-FEFD analysis, we used experimentally measured values of refractive index and THz-wave absorption coefficient (by field) of the nanoporous SiO_2 ; see Fig. 3(b). Finally, numerically modeled spatial distributions of the electromagnetic field intensity $I(\mathbf{r}) \sim \|\mathbf{E}(\mathbf{r})\|^2$ formed at the shadow side of the analyzed optical elements were compared with the experimental ones.

5. Experimental study of the nanoporous SiO_2 optical elements

The developed nanoporous SiO_2 -based THz optical elements were characterized experimentally using continuous-wave THz imaging. A home-made THz imaging system, featuring a backward-wave oscillator (BWO) [61] as a continuous-wave THz emitter with the output frequency of $\nu = 0.55$ THz, was used for optical characterization. This particular frequency corresponds to the local maximum in the BWO emission spectrum, and was also used in numerical analysis; see Sec. 4. Field intensity is recorded at the shadow side of an investigated optical element using a Golay cell [62], in front of which a small-diameter ($\leq \lambda$) diaphragm is mounted to achieve high spatial resolution. The Golay cell is mounted on a 3D linear translation stage with the

positioning accuracy of $\leq 2 \mu\text{m}$ and is used to record spatial distribution of the electromagnetic field intensity $I(\mathbf{r})$. In Fig. 4, we show schematic of an experimental setup, which is details in our prior works [36,63].

As shown in Fig. 4, in case of cylindrical lenses spatial distribution of the THz field intensity was recorded in the XOY plane, while for the axicon the intensity was measured in the XOZ plane. The origin $(0, 0, 0)$ is placed at the intersection point of a front surface of an optical element with optical (OZ) axis. In both cases, a linearly-polarized plane electromagnetic wave radiates an optical element from its convex side. In order to homogenise intensity of the BWO beam over the aperture, as well as to achieve the desired aperture of the beam, we applied a set of different polymethylpntnene (TPX) lenses. A TPX lens is placed after the BWO in order to collimate the THz beam. A pair of THz lenses form a telescopic system and results in a collimated THz beam with the diameter of $\approx 22 \text{ mm}$ (at the Full-Width at Half-Maximum – FWHM). Finally, a weakly-subwavelength diaphragm is placed in the focal plane of the telescope to homogenize the THz beam intensity over its aperture via diffraction [63], thus, increasing the beam quality.

6. Comparison of numerical and experimental data

In Figs. 5 and 6, the observed imaging data is compared with the results of 2D and 3D numerical simulations, as well as with the theoretical predictions based on the paraxial beam approximation.

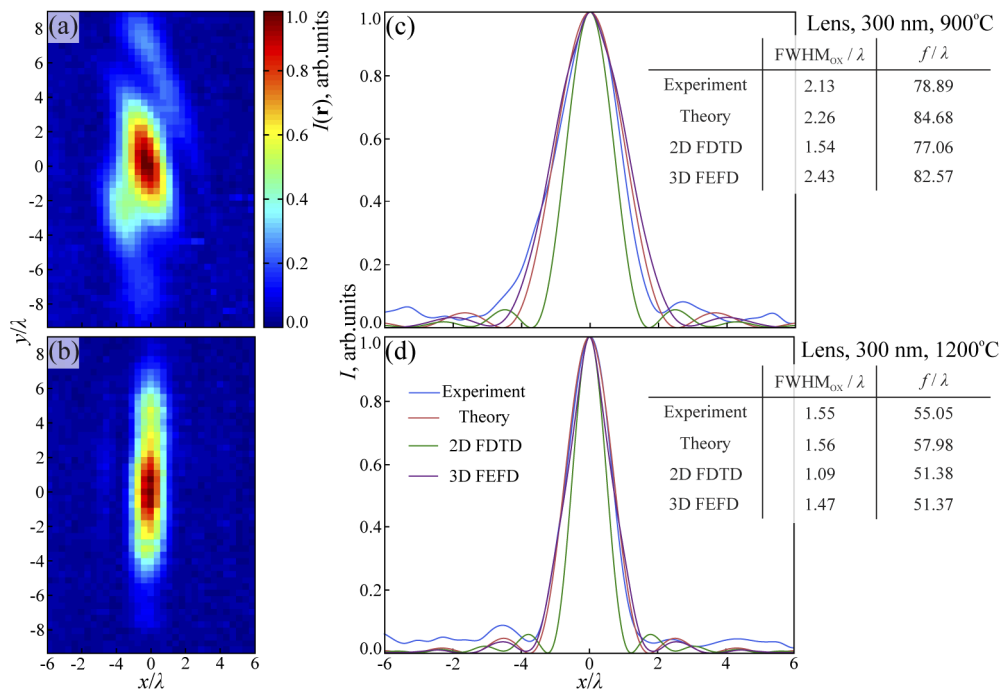


Fig. 5. Comparison of the experimental, numerical and theoretical results for the structures of the THz beam focused by the nanoporous SiO_2 -based cylindrical lenses at $\lambda = 545 \mu\text{m}$. (a),(b) Experimental images of the THz beam spots formed at the focal/image plane of the two cylindrical lenses annealed at 900°C and 1200°C , respectively. (c),(d) Intensity distributions of a beam spot at the focal plane along OX axis, including experimentally measured (blue), numerically computed 2D-FDTD (green) and 3D-FEFD (brown), and theoretically estimated (red). In the inserts of (c),(d), tables summarize the beam spot FWHM (in the OX direction) and the focal lengths for the considered lenses, as found by different methods.

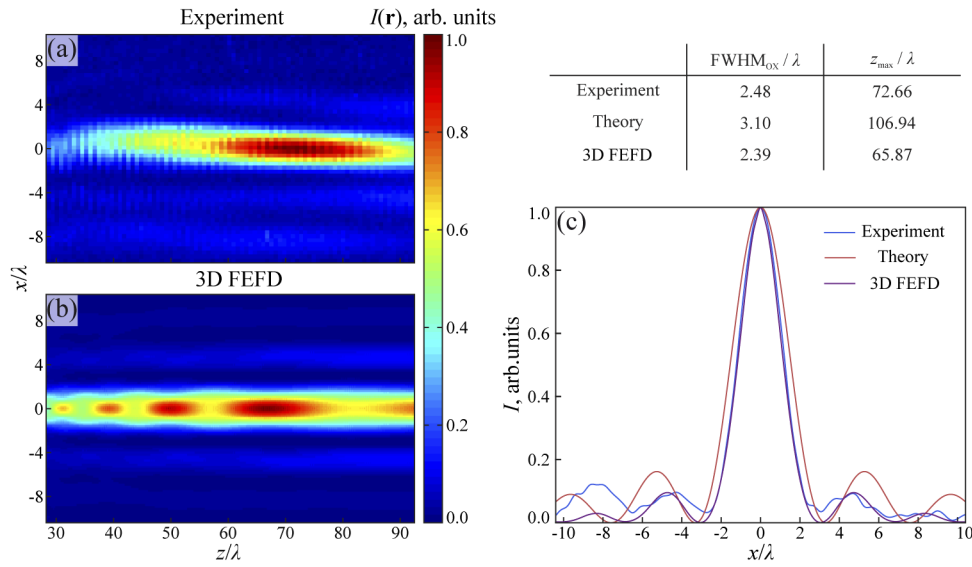


Fig. 6. Comparison of the experimental, numerical and theoretical data for the zero-order Bessel beam generated at $\lambda = 545 \mu\text{m}$ by an axicon made of nanoporous SiO_2 annealed at 950°C . (a),(b) Experimental and numerical (3D-FEFD) images of intensity distributions of a Bessel beam formed by an axicon. (c),(d) Experimentally-measured THz Bessel beam intensity along the OX direction, as compared with numerical simulations and theoretical predictions. Insert: a table summarizing experimental, numerical and theoretical results for the beam spot FWHM (in the OX direction) and the central longitudinal position of the Bessel beam z_{max} .

6.1. THz cylindrical lenses

In Figs. 5(a) and (b), we show experimental results of the THz field intensity distributions at the focal plane of the two cylindrical lenses made of nanoporous SiO_2 , that were annealed at 900°C and 1200°C , correspondingly. Experimental image plane was chosen to coincide with a focal plane ($z = f$), where field intensity along the optical (OZ) axis is maximal. As expected, strong localization of the focal spot intensity is observed along the OX direction due to THz beam focusing in this direction by the cylindrical optical surface. In turn, the size of a focal spot along the OY direction is much larger, which can be attributed to the diffraction of the THz beam at the lens aperture.

In Figs. 5(c) and (d), we present the THz beam spot cross-section along the OX direction for the two cylindrical lenses. The experimental data is overlapped with the results of numerical 2D-FDTD and 3D-FEFD simulations, as well as theoretical estimates. The theoretical focal lengths of the two lenses are calculated using the paraxial beam approximation for the plano-convex lens [64]

$$f = \frac{R}{n-1}, \quad (1)$$

where R is the curvature radius, and n is the refractive index of the lens, taken from the THz pulsed spectroscopy data at $\lambda = 545 \mu\text{m}$; see Fig. 3. The theoretical beam spot geometry can be estimated for the cylindrical lens relying on the scalar diffraction theory [65]

$$I(x) \propto \frac{\sin^2\left(\frac{R}{f\lambda}x\right)}{\left(\frac{R}{f\lambda}x\right)^2}. \quad (2)$$

From the inserts of Figs. 5(c),(d), we notice an overall good quantitative agreement between our experimental, theoretical and both 2D-FDTD and 3D-FEFD numerical considerations for the two cylindrical lenses.

The observed small-to-moderate discrepancies between experiment, numerical and theoretical data, including some asymmetry of the observed experimental beam spot (see Figs. 5(a) and (b)), might originate from a number of factors, such as non-ideal wavefront of a source wave, material density non-uniformity across sample, and inhomogeneous THz-wave absorption in material over the lens aperture. These effects are among the common reasons for the beam spot distortions in practical imaging systems [64]. Finally, the experimental image plane could be somewhat shifted with respect to a real focal plane.

Note that the two lenses made of nanoporous SiO₂ materials annealed at the temperatures of 900°C and 1200°C are characterized by different focal lengths ($f \approx 43$ mm and $f \approx 30$ mm) and beam spot sizes due to distinct values of refractive indices. Such a considerable difference in the lens optical properties highlight the versatility of the developed material platform for the THz bulk optics design.

6.2. THz axicon

In Figs. 6(a) and (b), results of the experimental and numerical (3D-FEFD) analysis of the zero-order Bessel beam generation using nanoporous SiO₂ axicon are presented. In our experiments, formation of the Bessel beam starts at the distances of ≈ 15 – 20 mm from the back optical surface of the axicon; while the focused beam extends up to the distance of ≈ 55 – 65 mm. Experimental and numerically-estimated width and longitudinal position (z_{\max}) of a Bessel beam maximum are quite similar. The latter can be also estimated using simple geometrical considerations [66]

$$z_{\max} = \frac{R}{2\gamma(n-1)}, \quad (3)$$

where n is a refractive index of the axicon material, and γ is an axicon refraction angle.

A notable discrepancy between the experimental data and simulations is associated with longitudinal oscillations of the Bessel beam intensity observed in the numerical data, as shown in Fig. 6(b). Such oscillations might originate due to THz beam diffraction at the axicone aperture, as well as longitudinal resonances inside the axicon, as detailed in Ref. [67]. At the same time, such oscillations were not observed in our experiments, which is attributed to the limited quality of the THz beam wavefront that irradiates the axicon.

In Fig. 6(c), experimentally measured cross-section of the Bessel beam intensity in the OX direction is compared with numerical simulations and theoretical estimates. The following model was applied to describe the beam spot of the observed Bessel beam [68]

$$I(r) \propto J_0^2\left(\frac{2\pi\sin(\beta)}{\lambda}r\right), \quad (4)$$

where r is a radius at the image plane, J_0 is the zero-order Bessel function and the angle β is a numerical aperture of the axicon and subject to the following constraint

$$n \cos(\theta/2) = \cos(\beta - \theta/2), \quad (5)$$

where θ is a apex angle of the axicon. From Fig. 6(c), we observe a good correspondence between experiment and numerical modeling, with only slight deviations in the position of a secondary maxima, as described by standard diffraction theory.

7. Discussion

The developed THz optical material platform makes it possible to produce a variety of bulk optical elements (such as lenses, windows, phase plates, prisms, or beam homogenizers)

using conventional mechanical processing techniques, such as grinding, polishing, or drilling. Moreover, optical elements with complex optical surfaces, such as diffracting optical elements, phase elements aimed at generation of complex-shaped optical beams, or even all-dielectric metasurfaces, can also be produced using direct sedimentation of aqueous colloidal suspension onto judiciously-designed molds. Spatial resolution of optical surfaces fabricated via this approach is generally limited by a sub-micron nanoparticle diameter, which is over three orders of magnitudes smaller than the THz wavelength. Additionally, thus fabricated nanoporous SiO₂ THz materials after annealing are generally environmentally stable [17]. Moreover, THz optical properties of the considered nanoporous SiO₂-based material can be tuned continuously over a wide range by annealing [17]. The technological robustness and tunability of the THz optical properties represent considerable advantages of the nanoporous SiO₂ material platform over conventional polymer and crystalline THz optical materials and, thus, improve our capabilities to design, synthesize and optimize THz optical elements and systems.

Direct sedimentation of colloidal suspensions onto optical surfaces followed by annealing can also be a promising approach for fabrication of the THz anti-reflection coatings of optical surfaces – a highly challenging problem due to limited diversity of the optical materials and deposition techniques [69]. Sedimentation technique can also be applied to the formation of cladding of solid- or hollow-core THz fibers and waveguides [70], and even multilayered structures for bandgap materials [24]. At the same time, development of such technology deserve further comprehensive studies, which is outside of the scope of this work.

Finally, in addition to using annealing in order to tune optical properties of nanoporous SiO₂ materials, as detailed in Ref. [69] and in this work, one can also implement other physical principles to manage their optical properties. For example, wide tunability of the material optical properties can be achieved by their doping with dielectric media, metallic (plasmonic) or magnetic nanoparticles, etc. Moreover, other nanoparticle types that are based on various polymers or even mixtures of several nanoparticle types can be used for the fabrication of THz materials [71]. In particular, an interesting and practically important material platform that can benefit from annealing technique for refractive index tunability is presented by porous silicon [72]. While promising, porous silicone at THz wavelengths tend to have conductivities (and, hence, absorption losses) that are much higher than that of HRFZ-Si, and thus, further research is needed to minimize losses in such porous materials.

8. Conclusion

In this paper, we discussed two different approaches for the fabrication of bulk THz optical elements relying on the novel material platform of THz optics – the artificial opals made of monodisperse SiO₂ nanoparticles, and annealed at different temperatures. First, conventional methods of mechanical processing were applied for producing the nanoporous SiO₂-based THz cylindrical lenses of identical geometry, but different refractive indices and focal lengths. Second, direct sedimentation of aqueous colloidal suspension of the SiO₂ nanoparticles onto a shaped substrate was used to fabricate a THz axicon. Thus fabricated bulk THz optical elements were studied numerically and experimentally. The observed results confirmed technological robustness of the developed THz optical material platform, thus, paving the way to creating a variety of bulk nanoporous SiO₂-based THz optical elements with complex shapes and tunable optical performance.

Funding. Canada Research Chairs (Ubiquitous Terahertz Photonics Project); Russian Science Foundation (19-12-00402).

Acknowledgements. The work of V.E. Ulitko, G.M. Katyba, V.N. Kurlov, and V.M. Masalov on fabrication and experimental study of nanoporous SiO₂ optical elements was supported by the Russian Science Foundation (Project # 19-12-00402). The work of M. Skorobogatiy on numerical simulations of the optical elements' performance was supported by the Canada Research Chairs Program (the Ubiquitous Terahertz Photonics Project).

Disclosures. The authors declare no conflicts of interest.

References

1. H. Guerboukha, K. Nallappan, and M. Skorobogatiy, "Toward real-time terahertz imaging," *Adv. Opt. Photonics* **10**(4), 843–938 (2018).
2. C. Walker, *Terahertz Astronomy*. 1st Edition (CRC Press, 2015).
3. B. Giuliano, A. Gavdush, B. Müller, K. Zaytsev, T. Grassi, A. Ivlev, M. Palumbo, G. Baratta, C. Scirè, G. Komandin, S. Yurchenko, and P. Caselli, "Broadband spectroscopy of astrophysical ice analogues - I. Direct measurement of the complex refractive index of CO ice using terahertz time-domain spectroscopy," *Astron. & Astrophys.* **629**, A112 (2019).
4. K. Zaytsev, I. Dolganova, N. Chernomyrdin, G. Katyba, A. Gavdush, O. Cherkasova, G. Komandin, M. Shchedrina, A. Khodan, D. Ponomarev, I. Reshetov, V. Karasik, M. Skorobogatiy, V. Kurlov, and V. Tuchin, "The progress and perspectives of terahertz technology for diagnosis of neoplasms: a review," *J. Opt.* **22**(1), 013001 (2020).
5. G. Musina, P. Nikitin, N. Chernomyrdin, I. Dolganova, A. Gavdush, G. Komandin, D. Ponomarev, A. Potapov, I. Reshetov, V. Tuchin, and K. Zaytsev, "Prospects of terahertz technology in diagnosis of human brain tumors – a review," *J. Biomed. Photonics Eng.* **6**(2), 020201 (2020).
6. D. Shao, P. Yotprayoosak, V. Saunajoki, M. Ahlskog, J. Virtanen, V. Kangas, A. Volodin, C. V. Haesendonck, M. Burdanova, C. D. W. Mosley, and J. Lloyd-Hughes, "Conduction properties of thin films from a water soluble carbon nanotube/hemicellulose complex," *Nanotechnology* **29**(14), 145203 (2018).
7. M. Burdanova, A. Tsapenko, D. Satco, R. Kashtiban, C. Mosley, M. Monti, M. Staniforth, J. Sloan, Y. Gladush, A. Nasibulin, and J. Lloyd-Hughes, "Giant negative terahertz photoconductivity in controllably doped carbon nanotube networks," *ACS Photonics* **6**(4), 1058–1066 (2019).
8. J. Zeitler, P. Taday, D. Newnham, M. Pepper, K. Gordon, and T. Rades, "Terahertz pulsed spectroscopy and imaging in the pharmaceutical setting - a review," *J. Pharm. Pharmacol.* **59**(2), 209–223 (2010).
9. Y. Tao, A. Fitzgerald, and V. Wallace, "Non-contact, non-destructive testing in various industrial sectors with terahertz technology," *Sensors* **20**(3), 712 (2020).
10. I. Dolganova, K. Zaytsev, S. Yurchenko, V. Karasik, and V. Tuchin, "The role of scattering in quasi-ordered structures for terahertz imaging: Local order can increase an image quality," *IEEE Trans. THz Sci. Technol.* **8**(4), 403–409 (2018).
11. A. Ren, A. Zahid, D. Fan, X. Yang, M. I. Ali, A. Alomainy, and Q. Abbasi, "State-of-the-art in terahertz sensing for food and water security – a comprehensive review," *Trends Food Sci. Technol.* **85**, 241–251 (2019).
12. A. Yachmenev, D. Lavrukhin, I. Glinitskiy, N. Zenchenko, Y. Goncharov, I. Spektor, R. Khabibullin, T. Otsuji, and D. Ponomarev, "Metallic and dielectric metasurfaces in photoconductive terahertz devices: a review," *Opt. Eng.* **59**, 061608 (2020).
13. A. Yachmenev, S. Pushkarev, R. Reznik, R. Khabibullin, and D. Ponomarev, "Arsenides and related III–V materials-based multilayered structures for terahertz applications," *Prog. Cryst. Growth Charact. Mater.* **66**(2), 100485 (2020).
14. Q. Sun, X. Chen, X. Liu, R. Stantchev, and E. Pickwell-MacPherson, "Exploiting total internal reflection geometry for terahertz devices and enhanced sample characterization," *Adv. Opt. Mater.* **8**(3), 1900535 (2020).
15. M. Manjappa and R. Singh, "Materials for terahertz optical science and technology," *Adv. Opt. Mater.* **8**(3), 1901984 (2020).
16. M. Islam, C. Cordeiro, M. Franco, J. Sultana, A. Cruz, and D. Abbott, "Terahertz optical fibers," *Opt. Express* **28**(11), 16089–16117 (2020).
17. V. Ulitko, A. Zotov, A. Gavdush, G. Katyba, G. Komandin, I. Spektor, I. Shmytko, G. Emelchenko, I. Dolganova, M. Skorobogatiy, V. Kurlov, V. Masalov, and K. Zaytsev, "Nanoporous SiO₂ based on annealed artificial opals as a favorable material platform of terahertz optics," *Opt. Mater. Express* **10**(9), 2100–2113 (2020).
18. A. Podzorov and G. Gallot, "Low-loss polymers for terahertz applications," *Appl. Opt.* **47**(18), 3254–3257 (2008).
19. B. Scherger, M. Scheller, C. Jansen, M. Koch, and K. Wiesauer, "Terahertz lenses made by compression molding of micropowders," *Appl. Opt.* **50**(15), 2256–2262 (2011).
20. K. Nielsen, H. Rasmussen, P. Uhd Jepsen, and O. Bang, "Porous-core honeycomb bandgap THz fiber," *Opt. Lett.* **36**(5), 666–668 (2011).
21. H. Bao, K. Nielsen, H. Rasmussen, P. Uhd Jepsen, and O. Bang, "Fabrication and characterization of porous-core honeycomb bandgap THz fibers," *Opt. Express* **20**(28), 29507–29517 (2012).
22. T. Ma, A. Markov, L. Wang, and M. Skorobogatiy, "Graded index porous optical fibers – dispersion management in terahertz range," *Opt. Express* **23**(6), 7856–7869 (2015).
23. F. Zhou, W. Cao, B. Dong, T. Reissman, W. Zhang, and C. Sun, "Additive manufacturing of a 3D terahertz gradient-refractive index lens," *Adv. Opt. Mater.* **4**(7), 1034–1040 (2016).
24. J. Li, K. Nallappan, H. Guerboukha, and M. Skorobogatiy, "3D printed hollow core terahertz Bragg waveguides with defect layers for surface sensing applications," *Opt. Express* **25**(4), 4126–4144 (2017).
25. M. Nazarov, A. Shilov, K. Bzheumikhov, Z. Margushev, V. Sokolov, A. Sotsky, and A. Shkurinov, "Eight-capillary cladding thz waveguide with low propagation losses and dispersion," *IEEE Trans. THz Sci. Technol.* **8**(2), 183–191 (2018).

26. T. Ma, H. Guerboukha, M. Girard, A. Squires, R. Lewis, and M. Skorobogatiy, "3D printed hollow-core terahertz optical waveguides with hyperuniform disordered dielectric reflectors," *Adv. Opt. Mater.* **4**(12), 2085–2094 (2016).
27. H. Guerboukha, K. Nallappan, Y. Cao, M. Seghilani, J. Azaña, and M. Skorobogatiy, "Planar porous components for low-loss terahertz optics," *Adv. Opt. Mater.* **7**(15), 1900236 (2019).
28. A. Dupuis, A. Mazhorova, F. Desevedavy, M. Roze, and M. Skorobogatiy, "Spectral characterization of porous dielectric subwavelength THz fibers fabricated using a microstructured molding technique," *Opt. Express* **18**(13), 13813–13828 (2010).
29. D. Grischkowsky, S. Keiding, M. van Exter, and C. Fattinger, "Far-infrared time-domain spectroscopy with terahertz beams of dielectrics and semiconductors," *J. Opt. Soc. Am. B* **7**(10), 2006–2015 (1990).
30. B. Chalmers, H. LaBelle, and A. Mlavsky, "Edge-defined, film-fed crystal growth," *J. Cryst. Growth* **13-14**, 84–87 (1972).
31. P. Antonov and V. Kurlov, "A review of developments in shaped crystal growth of sapphire by the Stepanov and related techniques," *Prog. Cryst. Growth Charact. Mater.* **44**(2), 63–122 (2002).
32. N. Abrosimov, V. Kurlov, and S. Rossolenko, "Automated control of Czochralski and shaped crystal growth processes using weighing techniques," *Prog. Cryst. Growth Charact. Mater.* **46**(1-2), 1–57 (2003).
33. G. Katyba, K. Zaytsev, I. Dolganova, I. Shikunova, N. Chernomyrdin, S. Yurchenko, G. Komandin, I. Reshetov, V. Nesvizhevsky, and V. Kurlov, "Sapphire shaped crystals for waveguiding, sensing and exposure applications," *Prog. Cryst. Growth Charact. Mater.* **64**(4), 133–151 (2018).
34. I. Minin, O. Minin, G. Katyba, N. Chernomyrdin, V. Kurlov, K. Zaytsev, L. Yue, Z. Wang, and D. Christodoulides, "Experimental observation of a photonic hook," *Appl. Phys. Lett.* **114**(3), 031105 (2019).
35. G. Katyba, D. Melikyants, N. Chernomyrdin, V. Kurlov, and K. Zaytsev, "Terahertz transmission-mode scanning-probe near-field optical microscopy based on a flexible step-index sapphire fiber," *Opt. Eng.* **60**(08), 082010 (2021).
36. K. Zaytsev, G. Katyba, N. Chernomyrdin, I. Dolganova, A. Rossolenko, V. Tuchin, V. Kurlov, and M. Skorobogatiy, "Overcoming the Abbe diffraction limit using a bundle of metal-coated high-refractive-index sapphire optical fibers," *Adv. Opt. Mater.* **8**(18), 2000307 (2020).
37. K. Zaytsev, G. Katyba, V. Kurlov, I. Shikunova, V. Karasik, and S. Yurchenko, "Terahertz photonic crystal waveguides based on sapphire shaped crystals," *IEEE Trans. THz Sci. Technol.* **6**(4), 576–582 (2016).
38. G. Katyba, K. Zaytsev, N. Chernomyrdin, I. Shikunova, G. Komandin, V. Anzin, S. Lebedev, I. Spektor, V. Karasik, S. Yurchenko, I. Reshetov, V. Kurlov, and M. Skorobogatiy, "Sapphire photonic crystal waveguides for terahertz sensing in aggressive environments," *Adv. Opt. Mater.* **6**(22), 1800573 (2018).
39. G. Katyba, K. Zaytsev, I. Dolganova, N. Chernomyrdin, V. Ulitko, S. Rossolenko, I. Shikunova, and V. Kurlov, "Sapphire waveguides and fibers for terahertz applications," *Prog. Cryst. Growth Charact. Mater.* **67**(3), 100523 (2021).
40. D. Han, K. Lee, J. Lim, S. Hong, Y. Kim, and J. Ahn, "Terahertz lens made out of natural stone," *Appl. Opt.* **52**(36), 8670–8675 (2013).
41. M. Nazarov, E. Khaydukov, A. Savelyev, V. Sokolov, A. Akhmanov, A. Shkurinov, and V. Panchenko, "Terahertz response of a polymer composite with high concentration of silicon micro- and nanoparticles," *Nanotechnol. Russ.* **10**(3-4), 247–253 (2015).
42. M. Wichmann, A. Mondol, N. Kocic, S. Lippert, T. Probst, M. Schwerdtfeger, S. Schumann, T. Hochrein, P. Heidemeyer, M. Bastian, G. Bastian, and M. Koch, "Terahertz plastic compound lenses," *Appl. Opt.* **52**(18), 4186–4191 (2013).
43. M. Sindler, C. Kadlec, F. Dominec, P. Kuzel, C. Elissalde, A. Kassas, J. Lesseur, D. Bernard, P. Mounaix, and H. Nemeč, "Bulk magnetic terahertz metamaterials based on dielectric microspheres," *Opt. Express* **24**(16), 18340–18345 (2016).
44. A. Nakanishi and H. Satozono, "Terahertz optical properties of wood–plastic composites," *Appl. Opt.* **59**(4), 904–909 (2020).
45. V. Ulitko, A. Zotov, A. Gavdush, G. Katyba, G. Komandin, I. Spektor, V. Kurlov, V. Masalov, and K. Zaytsev, "Novel promising terahertz optical material based on nanoporous SiO₂," *Proc. SPIE* **11499**, 1149915 (2020).
46. V. Ulitko, A. Zotov, V. Masalov, G. Emelchenko, G. Katyba, V. Kurlov, and K. Zaytsev, "Novel elements of terahertz optics based on artificial opals," *J. Surf. Investig. X-ray Synchrotron & Neutron Tech.* (2021, in press).
47. K. Hartlen, A. T. Athanasopoulos, and V. Kitaev, "Facile preparation of highly monodisperse small silica spheres (15 to >200 nm) suitable for colloidal templating and formation of ordered arrays," *Langmuir* **24**(5), 1714–1720 (2008).
48. V. Masalov, N. Sukhinina, and G. Emelchenko, "Colloidal particles of silicon dioxide or the formation of opal-like structures," *Phys. Solid State* **53**(6), 1135–1139 (2011).
49. K. Davis, W. Russel, and W. Glantschnig, "Settling suspensions of colloidal silica: Observations and X-ray measurements," *J. Chem. Soc., Faraday Trans.* **87**(3), 411–424 (1991).
50. G. Sokolovskii, V. Dudelev, S. Losev, K. Soboleva, A. Deryagin, K. Fedorova, V. Kuchinskii, W. Sibbett, and E. Rafailov, "Bessel beams from semiconductor light sources," *Prog. Quantum Electron.* **38**(4), 157–188 (2014).
51. O. Brzobohaty, T. Cizmar, and P. Zemanek, "High quality quasi-Bessel beam generated by round-tip axicon," *Opt. Express* **16**(17), 12688–12700 (2008).
52. G. Komandin, V. Anzin, V. Ulitko, A. Gavdush, A. Mukhin, Y. Goncharov, O. Porodinkov, and I. Spektor, "Optical cryostat with sample rotating unit for polarization-sensitive terahertz and infrared spectroscopy," *Opt. Eng.* **59**(6), 061603 (2020).

53. G. Musina, I. Dolganova, N. Chernomyrdin, A. Gavdush, V. Ulitko, O. Cherkasova, D. Tuchina, P. Nikitin, A. Alekseeva, N. Bal, G. Komandin, V. Kurlov, V. Tuchin, and K. Zaytsev, "Optimal hyperosmotic agents for tissue immersion optical clearing in terahertz biophotonics," *J. Biophotonics* **13**(12), e202000297 (2020).
54. D. Lavrukhin, A. Yachmenev, A. Pavlov, R. Khabibullin, Y. Goncharov, I. Spektor, G. Komandin, S. Yurchenko, N. Chernomyrdin, K. Zaytsev, and D. Ponomarev, "Shaping the spectrum of terahertz photoconductive antenna by frequency-dependent impedance modulation," *Semicond. Sci. Technol.* **34**(3), 034005 (2019).
55. K. Zaytsev, A. Gavdush, V. Karasik, V. Alekhnovich, P. Nosov, V. Lazarev, I. Reshetov, and S. Yurchenko, "Accuracy of sample material parameters reconstruction using terahertz pulsed spectroscopy," *J. Appl. Phys.* **115**(19), 193105 (2014).
56. I. Pupeza, R. Wilk, and M. Koch, "Highly accurate optical material parameter determination with THz time-domain spectroscopy," *Opt. Express* **15**(7), 4335–4350 (2007).
57. J. B. Schneider, *Understanding the Finite-Difference Time-Domain Method* (2010).
58. K. Yee and J. Chen, "The finite-difference time-domain (FDTD) and the finite-volume time-domain (FVTD) methods in solving Maxwell's equations," *IEEE Trans. Antennas Propagat.* **45**(3), 354–363 (1997).
59. K. Umashankar and A. Taflov, "A novel method to analyze electromagnetic scattering of complex objects," *IEEE Trans. Electromagn. Compat.* **EMC-24**(4), 397–405 (1982).
60. M. Albani and P. Bernardi, "A Numerical Method Based on the Discretization of Maxwell Equations in Integral Form (Short Papers)," *IEEE Trans. Microwave Theory Tech.* **22**(4), 446–450 (1974).
61. G. Komandin, S. Chuchupal, S. Lebedev, Y. Goncharov, A. Korolev, O. Porodinkov, I. Spektor, and A. Volkov, "BWO generators for terahertz dielectric measurements," *IEEE Trans. THz Sci. Technol.* **3**(4), 440–444 (2013).
62. H. Zahl and M. Golay, "Pneumatic heat detector," *Rev. Sci. Instrum.* **17**(11), 511–515 (1946).
63. N. V. Chernomyrdin, A. S. Kucheryavenko, G. S. Kolontaeva, G. M. Katyba, I. N. Dolganova, P. A. Karalkin, D. S. Ponomarev, V. N. Kurlov, I. V. Reshetov, M. Skorobogatiy, V. V. Tuchin, and K. I. Zaytsev, "Reflection-mode continuous-wave 0.15 λ -resolution terahertz solid immersion microscopy of soft biological tissues," *Appl. Phys. Lett.* **113**(11), 111102 (2018).
64. M. Born and E. Wolf, *Principles of optics: Electromagnetic theory of propagation, interference and diffraction of light. 7th Edition* (Cambridge University Press, 1999), 7th ed.
65. C. J. R. Sheppard, "Cylindrical lenses-focusing and imaging: A review [Invited]," *Appl. Opt.* **52**(4), 538–545 (2013).
66. M. Anguiano-Morales, "Transformation of Bessel beams by means of a cylindrical lens," *Appl. Opt.* **48**(25), 4826–4831 (2009).
67. P. L. Overfelt and C. S. Kenney, "Comparison of the propagation characteristics of Bessel, Bessel-Gauss, and Gaussian beams diffracted by a circular aperture," *J. Opt. Soc. Am. A* **8**(5), 732 (1991).
68. R. Arimoto, C. Saloma, T. Tanaka, and S. Kawata, "Imaging properties of axicon in a scanning optical system," *Appl. Opt.* **31**(31), 6653–6657 (1992).
69. A. Gavdush, N. Chernomyrdin, D. Lavrukhin, Y. Cao, G. Komandin, I. Spektor, A. Perov, I. Dolganova, G. Katyba, V. Kurlov, D. Ponomarev, M. Skorobogatiy, I. Reshetov, and K. Zaytsev, "Proof of concept for continuously-tunable terahertz bandpass filter based on a gradient metal-hole array," *Opt. Express* **28**(18), 26228–26238 (2020).
70. R. A. Caruso, J. H. Schattka, and A. Greiner, "Titanium dioxide tubes from sol-gel coating of electrospun polymer fibers," *Adv. Mater.* **13**(20), 1577–1579 (2001).
71. R. Rozenberg and B. A. Tenne, "Polymer-assisted fabrication of nanoparticles and nanocomposites," *Prog. Polym. Sci.* **33**(1), 40–112 (2008).
72. K. Dadzis, R. Menzel, U. Juda, K. Irmischer, C. Kranert, M. Müller, M. Ehrl, R. Weingärtner, C. Reimann, H. Abrosimov, and N. Riemann, "Characterization of silicon crystals grown from melt in a granulate crucible," *J. Electron. Mater.* **49**(9), 5120–5132 (2020).